Journal of Solid State Chemistry xxx (xxxx) 123512

Contents lists available at ScienceDirect

Journal of Solid State Chemistry

journal homepage: www.elsevier.com/locate/jssc

Electron doping of $NdNiO_3$ thin films using dual chamber CaH_2 annealing

Dinesh K. Amarasinghe [a], Haoming Yu [a], Fanny Rodolakis [b], Hua Zhou [b], Hui Cao [c], Shriram Ramanathan [a, *]

[a] School of Materials Engineering, Purdue University, West Lafayette, IN, 47907, USA
[b] X-ray Science Division, Advanced Photon Source, Argonne National Laboratory, Lemont, IL, 60439, USA
[c] Materials Science Division, Argonne National Laboratory, Lemont, IL, 60439, USA

ARTICLE INFO

Keywords:
$NdNiO_3$ thin films
$LaAlO_3$
CaH_2 annealing
Electron doping
Hydrogenation
Mott transition

ABSTRACT

Hydrogen donor doping has been exploited as a strategy to manipulate the electronic structure and electrical properties of functional oxide systems. Especially, the development of synthetic methods to achieve electron doping of perovskite rare-earth nickelate thin films utilizing interstitial hydrogen is highly desirable considering the rich electronic phase diagram hosting several functional properties. In this work, we present the hydrogenation of $NdNiO_3$ (NNO) thin films using CaH_2 annealing and the resulting giant modulation of electrical resistivity in hydrogenated NNO (H–NNO) thin films. Magnetron sputtering was employed to deposit epitaxial ~60 nm-thin NNO films on single crystal $LaAlO_3$ (LAO) substrates. The formation of the pristine perovskite NNO phase was realized after annealing the films at 500 °C for 24 h. CaH_2 annealing of NNO thin films for time durations ranging from 1 to 6 h was performed in a vacuumed ampule with two interconnected chambers at 280 °C. The two-chamber design enables a simple and clean approach for hydrogen doping without physical contact between the powder and sample of interest. X-ray diffraction and Raman spectroscopy revealed the formation of NNO in pristine samples, and the subsequent hydrogen incorporation upon CaH_2 annealing without forming any impurity phases. The conversion of the oxidation state of Ni towards +2 upon CaH_2 annealing was probed using X-ray photoelectron spectroscopy and X-ray absorption spectroscopy. Consequently, a substantial increase in the room-temperature resistivity was observed upon CaH_2 annealing indicating the formation of a strongly correlated electronic configuration of Ni in H–NNO due to electron doping. Overall, the findings of this study highlight the versatility of CaH_2 annealing as an electron doping method to tune the electrical properties of correlated oxides at low temperatures.

1. Introduction

Perovskite rare-earth nickelates with the generic formula $RENiO_3$ (RE = rare-earth) constitute an important class of correlated oxides, which have been widely investigated for their temperature driven metal–insulator transition (MIT) [1–3]. Manipulation of the electronic structure and the resulting electrical properties of rare-earth nickelate thin films by carrier doping is of interest across fundamental materials research and computing [4–9]. To this end, electron doping of $RENiO_3$ by changing the interstitial defect density and cation valence states has gained widespread research interest. Upon electron doping such as from hydrogen, nominal Ni^{3+} ions in NiO_6 octahedra in undoped $RENiO_3$ are reduced to Ni^{2+} ions leading to a highly insulating state. Electron doping approaches utilized on rare-earth nickelates to yield a large modulation in electrical resistivity at room temperature include intercalation of H^+ and Li^+ ions, substitution of F^- for O^{2-}, and introducing oxygen deficiency [5,10–14]. In this context, the development of additional synthetic methods to achieve electron doping of rare-earth nickelates and other correlated oxides is highly desirable considering the potential of these materials as a platform for adaptive, tunable matter.

Search for synthetic methods for electron doping of rare-earth nickelates points to the recent use of CaH_2 annealing for electron doping of perovskite $BaZrO_3$ thin films [15]. In fact, CaH_2 annealing has been used as a facile low-temperature topochemical reaction route to synthesize metastable phases, which are not accessible by conventional high-temperature solid-state reactions [16]. Topochemical reduction of perovskite rare-earth nickelate thin films by CaH_2 annealing has provided synthetic access to superconducting infinite-layer phases including $Nd_{0.8}Sr_{0.2}NiO_2$ and $Pr_{0.8}Sr_{0.2}NiO_2$ [17,18]. In these cases, CaH_2 acts as a

* Corresponding author.
E-mail address: shriram@purdue.edu (S. Ramanathan).

https://doi.org/10.1016/j.jssc.2022.123512
Received 3 July 2022; Received in revised form 15 August 2022; Accepted 16 August 2022

reducing agent and removes apical oxide anions from the perovskite crystal structure of $RENiO_3$. In addition, it has been shown that incorporation of hydride anions by CaH_2 annealing enables the synthesis of oxyhydride phases such as $SrVO_2H$, $LaSrCoO_3H_{0.7}$, $SrCoO_xH_y$, and $ATiO_{3-x}H_x$ (A = Ba, Sr, and Ca) in thin film forms [19–22]. Onozuka and coworkers investigated the effect of CaH_2 annealing on $NdNiO_3$ (NNO) thin films deposited on $SrTiO_3$ (STO) substrate and reported the formation of the oxyhydride $NdNiO_xH_y$ [23]. In addition, theoretical studies have recognized CaH_2 annealing as a feasible synthetic route for incorporating hydrogen into nickelates [24,25]. Annealing experiments carried out with CaH_2 and metal oxides as well as the thermal desorption spectroscopic investigations have shown that CaH_2 may act as an *in-situ* source of H_2 gas [26–28]. In fact, the generation of *in-situ* H_2 has been realized at low temperatures (250–300 °C) to facilitate topochemical reduction and hydrogenation reactions. Motivated by the findings of above studies, we aimed at examining the effect of CaH_2 annealing on NNO thin films deposited on $LaAlO_3$ (LAO) substrate.

In this article, we report the synthesis, characterization, and electrical transport properties of hydrogen-doped NNO (H–NNO) thin films obtained by CaH_2 annealing. A novel experimental set up for annealing NNO thin films with a physically separated CaH_2 chamber has been introduced. The changes in the crystal structure of NNO and valence state of Ni upon hydrogenation have been probed using X-ray diffraction and X-ray spectroscopy, respectively. We also demonstrate the conversion of the correlated metal NNO to a highly insulating state at room temperature by hydrogen incorporation *via* CaH_2 annealing. The broad applicability of CaH_2 annealing as an electron doping strategy to modulate the electrical transport properties of correlated oxides is highlighted.

2. Experimental

2.1. Deposition of NNO thin films

Epitaxial NNO thin films (~60 nm) were grown on (001) LAO substrate employing reactive magnetron sputtering followed by post annealing in air. Co-sputtering from Nd (RF, 135 W) and Ni (DC, 80 W) targets in an Ar/O_2 atmosphere was first performed on the substrate at room temperature. Flow rates of Ar and O_2 were 40 and 10 SCCM, respectively. Deposition was carried out for 30 min at a total pressure of 5 mTorr. The formation of the pristine perovskite NNO phase was realized after annealing the films in a tube furnace at 500 °C for 24 h in air. Total ramping time was 10 h (5 h each for heating and cooling).

2.2. Topochemical reduction

As shown in Fig. 1, a pristine NNO thin film was loaded into an encapsulation vessel with CaH_2 powder inside of an argon filled glovebox. Approximately 0.5 g of CaH_2 powder was used for a 5 × 5 mm^2 NNO film. CaH_2 powder and NNO thin film were placed in different interconnected chambers in the encapsulation vessel to ensure a complete gas phase hydrogenation reaction. Encapsulation vessel was closed using an encapsulation vessel adapter and the glassware assembly was taken out of the glovebox. The glassware assembly was then evacuated to a pressure of 2×10^{-4} Torr and carefully sealed to obtain a glass ampule with the two interconnected chambers containing the NNO thin film and CaH_2 powder. The separation between the two chambers was kept fixed at ~6 mm. Then, the glass ampule was placed in a tube furnace and annealed at 280 °C; annealing time was varied in the 1–12 h range. Heating and cooling rates of 10 °C/min were used. After the annealing step, H–NNO thin films were rinsed thoroughly with deionized water, ethanol, and isopropanol and used for further characterization.

2.3. X-ray diffraction (XRD)

Room-temperature XRD patterns of LAO, NNO, and H–NNO films were collected using a Panalytical MRD X'Pert Pro high-resolution diffractometer with Cu Kα radiation (λ = 1.5406 Å).

2.4. Synchrotron X-ray reflectivity (XRR), diffraction, and reciprocal space mapping (RSM)

Synchrotron XRR, XRD, and RSM measurements of the NNO and H–NNO thin film samples were carried out on a six-circle Huber diffrac-

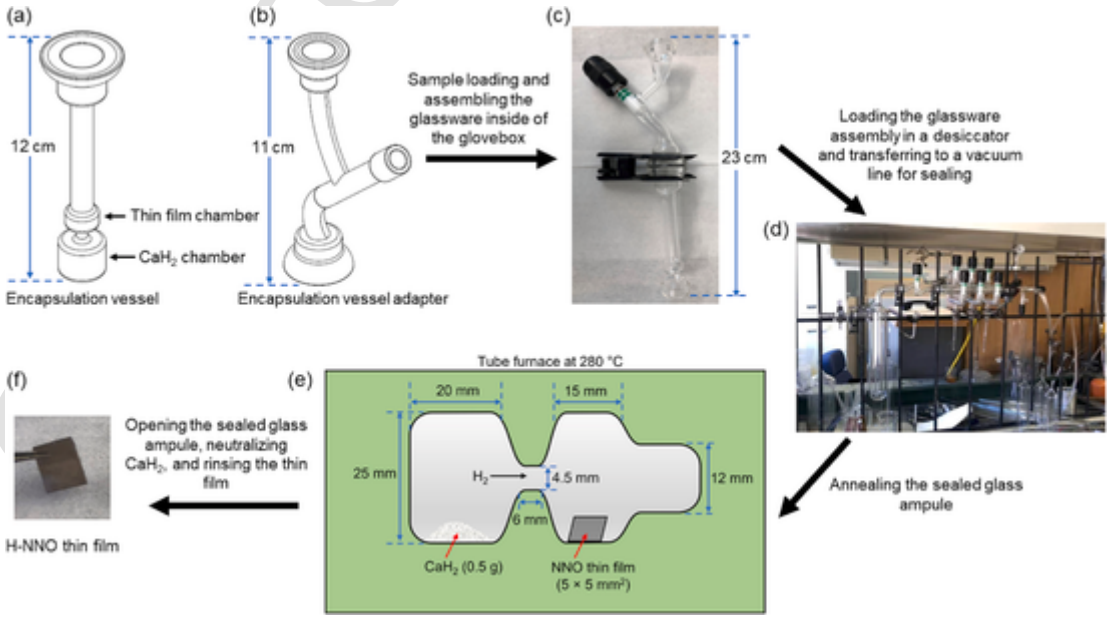

Fig. 1. Schematic illustration of the process flow of CaH_2 annealing of NNO thin films. (a) Encapsulation vessel with two interconnected chambers for NNO thin film and CaH_2. (b) Encapsulation vessel adapter used for closing the encapsulation vessel after loading NNO thin film and CaH_2 powder. (c) Assembly of the encapsulation vessel and adapter before vacuum sealing. (d) Vacuum line used for evacuating the glassware assembly and sealing to obtain the glass ampule. (e) Glass ampule with two interconnected chambers containing NNO thin film and CaH_2 powder for annealing at 280 °C. (f) H–NNO thin film obtained after CaH_2 annealing.

tometer with psi-c geometry using an X-ray energy of 20 keV (λ = 0.6199 Å) at the beamline sector 33-BM-C in the Advanced Photon Source (APS) at the Argonne National Laboratory. A Si (111) double crystal monochromator with a resolution $\Delta E/E = 1 \times 10^{-4}$ was used to modulate and set X-ray energy. The X-ray beam had a total flux of 1×10^{11} photons/s at 20 keV, and the beam was vertically focused by a vertically focusing mirror. The double crystal monochromator used a sagittal focusing crystal for horizontal focusing. An X-ray beam profile of 300 μm (V) × 500 μm (H) was used in the measurement. Geometric corrections and background subtractions were applied for all XRR and XRD data. RSM data were processed by the RSMap3D software developed by APS.

2.5. Raman Spectroscopy

Raman spectra were measured at room temperature using a Renishaw inVia Raman spectrometer. Acquisition of spectra was carried out in the backscattering geometry employing an excitation wavelength of 532 nm with a power of 1 mW.

2.6. X-ray photoelectron spectroscopy (XPS)

High-resolution XPS spectra of NNO and H–NNO thin films were obtained using a Kratos X-ray Photoemission Spectrometer and monochromatic Al Kα radiation (1486.6 eV) as the excitation source. The binding energies of XPS spectra were calibrated according to the binding energy of C 1*s* peak (284.8 eV).

2.7. X–ray absorption spectroscopy (XAS)

O *K* edge and Ni *L* edge XAS data of pristine NNO and selected H–NNO samples were collected at beamline 29-ID-D of the Advanced Photon Source at Argonne National Laboratory. Data were measured simultaneously in total electron yield (TEY) and total fluorescence yield (TFY) at room temperature in a pressure of 5×10^{-8} Torr. TFY signal was collected using a silicon drift diode detector (Vortex) located at 155° from direct beam. The incidence angle was set to 15°. Circular polarized X-ray with an overall energy resolution better than 100 meV was used. Using the drain current from a gold mesh upstream of the sample, both absorption signals were normalized by the incident X-ray intensity.

2.8. Electrical transport property measurements

Temperature-dependent resistivity measurements were performed utilizing a Quantum Design physical property measurement system (PPMS). NNO and H–NNO thin films were mounted on a puck and connected with Au contacts. A small excitation AC signal (1 μA) was employed for the measurements. Measurements were performed in the four-probe configuration.

3. Results and discussion

XRD patterns and Raman spectra were taken from NNO thin films on LAO substrate and structural evolution of H–NNO thin films as a function of CaH_2 annealing temperature and time was monitored. Results from these investigations are summarized in Fig. 2. As shown in Fig. 2a, the successful deposition of pristine NNO on LAO substrate is confirmed by the appearance of the distinct diffraction maxima at 47.5°, which corresponds to the (002) reflection of pseudo-cubic NNO. An out-of-plane lattice constant (c_{NNO}) of ~3.825 Å was also extracted from these measurements. This slight expansion of the unit cell along the *c* axis compared to the corresponding value in bulk NNO (3.807 Å) may be a result of the in-plane compressive stress introduced by the LAO substrate [29,30]. More importantly, XRD studies confirmed that the sputtering and post annealing conditions utilized in this study lead to the growth of *c*-axis oriented pristine NNO films on LAO substrate without any detectable impurity phases. Next, a series of experiments was carried out to ascertain the optimum temperature for CaH_2 annealing to realize electron doping. Targeted annealing temperatures were 200, 280, and 400 °C; annealing time was kept fixed at 3 h. The presence/degradation of the NNO phase on LAO substrate after CaH_2 annealing at these temperatures was probed using XRD and degree of hydrogen incorporation was qualitatively monitored using Raman Spectroscopy. The distinct diffraction maximum at 47.5° corresponding to (002) reflection of pseudo-cubic NNO was clearly observed in the XRD patterns collected after CaH_2 annealing at 200 and 280 °C indicating the preservation of NNO phase after CaH_2 annealing at these temperatures. In contrast, the absence of a peak at ~47.5° in the XRD pattern implied the degradation of NNO thin film annealed with CaH_2 at 400 °C for 3 h. Therefore, in this study, temperatures ≥400 °C were considered to be harsh for CaH_2 annealing of NNO thin films. Raman spectra were collected to confirm the incorporation of hydrogen into the crystal structure of NNO after CaH_2 annealing at 200, 280, and 400 °C. As shown in Fig. 2b, the Raman peak at ~487 cm^{-1} originates from the E_g vibration of LAO substrate [31]. Pristine NNO usually exhibits 24 Raman modes. However, only a limited number of Raman vibrations are experimentally observed. A Raman peak from the T_{2g} mode of pristine NNO is observed at ~433 cm^{-1} [32]. It has been reported that the intensity of this peak is sensitive to the hydrogen incorporation [33,34]. In comparison to the intensity of the Raman peak at ~433 cm^{-1} in pristine NNO, no significant change in the intensity of the corresponding peak in the NNO thin film annealed at 200 °C was noticed. This behavior may originate due to no hydrogen incorporation into NNO lattice at low CaH_2 annealing temperatures (≤200 °C). However, the disappearance of the Raman peak at ~433 cm^{-1} upon CaH_2 annealing at 280 °C for 3 h suggested the hydrogen doping of NNO without degrading the perovskite crystal structure. Therefore, 280 °C was chosen as the optimum CaH_2 annealing temperature of NNO thin films in our study. In addition, we probed the effect of vacuum annealing of NNO thin films at 280 °C for 3 h; no significant change in the intensity of the Raman peak at ~433 cm^{-1} was noticed (Electronic Supporting Information, ESI-Fig. 1). On the other hand, annealing NNO thin films patterned with Pt electrodes in 5% H_2/95% Ar forming gas at 125 °C for 10 min led to the disappearance of the Raman peak at ~433 cm^{-1}. Noticeably, it has been reported that hydrogen doping by electrochemical method and annealing with 5% H_2/95% Ar forming gas leads to a similar suppression of the intensity of the corresponding Raman peak in hydrogenated perovskite $RENiO_3$ [31,33,34]. Hence, it is reasonable to conclude that H_2 doping by CaH_2 annealing as the primary origin of the suppression of the intensity of the Raman peak at ~433 cm^{-1} and resulting increase in the resistivity of H–NNO thin films (*vide infra*) in the current study. Having optimized the CaH_2 annealing temperature, we then systematically change the CaH_2 annealing time at 280 °C to study the structural evolution of H–NNO samples. As depicted in Fig. 2C, a slight shift of the (002) diffraction maximum of NNO to lower angle is observed upon CaH_2 annealing for 4 h at 280 °C. This corresponds to ~0.7% expansion of the out-of-plane lattice constant due to the strain induced by hydrogen doping (ESI-Fig. 2). Upon CaH_2 annealing for 2 h, the intensity of the Raman peak at ~433 cm^{-1} strongly decreased confirming the hydrogen doping of NNO thin films (Fig. 2d). According to the reports on topochemical reduction of NNO thin films grown on $SrTiO_3$ (STO) by CaH_2 annealing, the formation of infinite layer $NdNiO_2$ phase is confirmed by the appearance of a XRD peak at ~55° [17,23,35]. However, we noticed no new peak in the corresponding region of the XRD patterns of our H–NNO samples suggesting the absence of $NdNiO_2$ phase. It should be noticed that the complete stabilization of $NdNiO_2$ on STO required a protective capping layer while no LAO capping layer was utilized in our investigation [17,35]. In addition, no peaks corresponding to oxyhydride $NdNiO_xH_y$ were present in the diffraction patterns of our

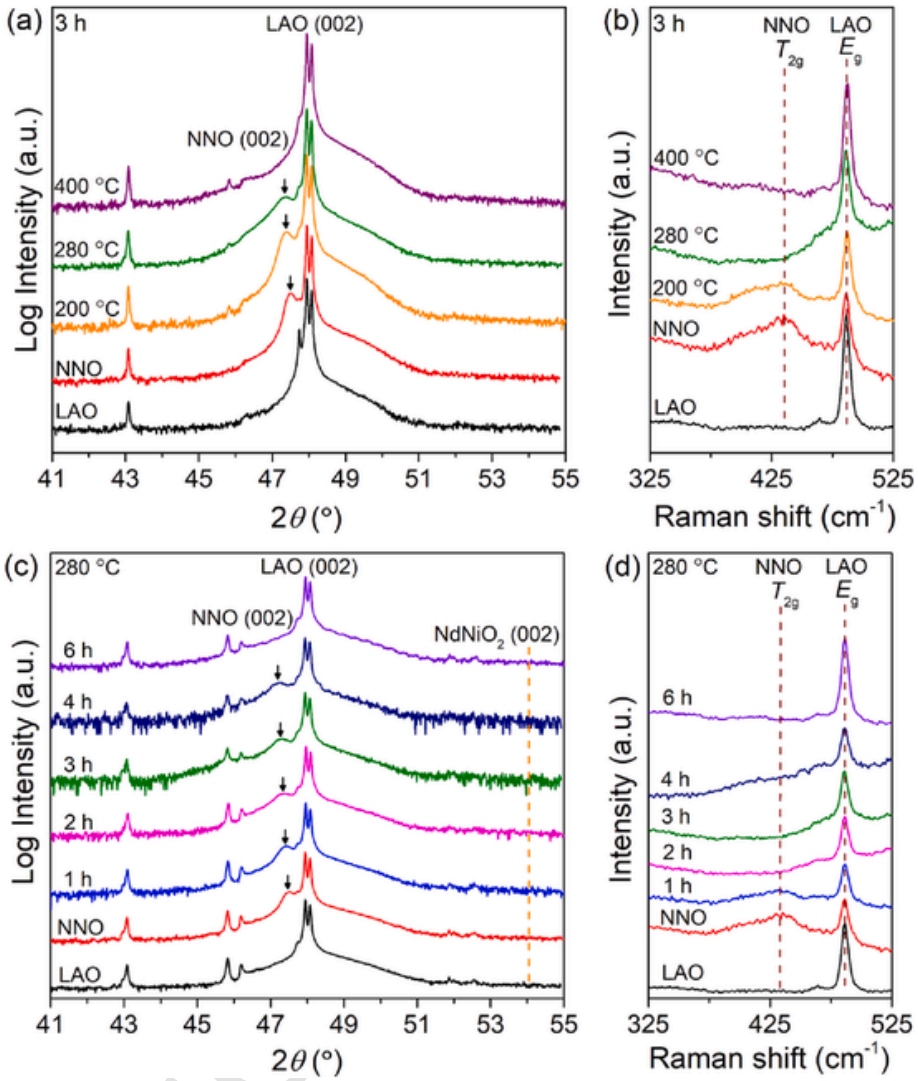

Fig. 2. (a) XRD patterns and (b) Raman spectra of LAO substrate, NNO thin film, and NNO thin films annealed for 3 h at 200, 280, and 400 °C with CaH_2. (c) XRD patterns and (d) Raman spectra of LAO substrate, NNO thin film, and NNO thin films annealed at 280 °C for 1, 2, 3, 4, and 6 h with CaH_2. (002) reflection of LAO is labeled in (a) and (c). (002) reflection of NNO is labeled with pseudocubic notation and indicated by an arrow in (a) and (c). Dashed line in (c) corresponds to the expected (002) XRD peak position of $NdNiO_2$. Dashed lines in (b) and (d) denote the Raman peak maxima of LAO and NNO located at ~487 and 433 cm^{-1}, respectively. The NNO peak intensity decreased after hydrogen doping by CaH_2 annealing.

study [23]. More importantly, the absence of any additional diffraction peaks corresponding to secondary crystalline phases in our samples suggests that CaH_2 annealing for 1–4 h causes no significant changes in the crystal structure of NNO thin films deposited on LAO except for the lattice expansion. The diminished intensity of the (002) XRD peak revealed that the prolonged annealing with CaH_2 for 6 h induces the structural degradation of NNO thin films. As shown in ESI-Fig. 3a, a re-annealing experiment was performed at 500 °C for 24 h in air on the degraded thin films obtained from CaH_2 annealing at 280 °C for 6 h. Interestingly, (002) diffraction maximum of NNO was observed in the XRD pattern of the re-annealed sample revealing the recovery of the perovskite NNO structure upon exposure to air at 500 °C. A similar outcome was observed in the re-annealing experiment carried out on the degraded NNO thin films obtained from CaH_2 annealing at 280 °C for 12 h (ESI-Fig. 3b). Overall, these results highlighted the importance of using shorter reaction times (1–4 h) at 280 °C to achieve hydrogen doping of NNO thin films on LAO substrate by CaH_2 annealing.

The role of hydrogen doping during CaH_2 annealing was determined using a series of current-voltage (I–V) measurements on NNO samples annealed under different conditions. Results from this analysis are shown in ESI-Fig. 4. Room-temperature resistance of NNO thin films patterned with Pt electrodes was significantly enhanced from ~144 to ~13850 Ω upon annealing in 5% H_2/95% Ar forming gas at 125 °C for 10 min (ESI-Fig. 4a). More importantly, room-temperature resistance reached a colossal value of ~725000 Ω after annealing NNO thin films patterned with Pt electrodes at 280 °C for 3 h with CaH_2. This observation (i.e. catalytic electrode-enhanced massive resistance increase) strongly implies that the generation of *in-situ* H_2 and hydrogen doping of NNO thin films indeed occur during CaH_2 annealing. As depicted in ESI-Fig. 4b, annealing pristine NNO films without Pt electrodes in 5% H_2/95% Ar forming gas at 125 °C for 10 min led to a minor increase in the film resistance demonstrating the importance of catalytic activity of Pt towards hydrogen incorporation. In addition, the resistance of the sample annealed in 5% H_2/95% Ar with Pt electrodes (~13850 Ω) could be lowered to that of the pristine NNO by re-annealing the hydrogenated films at 200 °C for 15 min in air indicating the relatively weak binding of hydrogen in NNO lattice. It has also been shown that hydrogen incorporation under these annealing conditions takes place as H^+ ions in interstitial sites of the NNO lattice [5,6]. On the other hand, annealing pristine NNO thin films at 280 °C for 3 h with CaH_2 resulted in a room-temperature resistance of ~88600 Ω whereas the corresponding value reached after performing the same experiment with no CaH_2 was

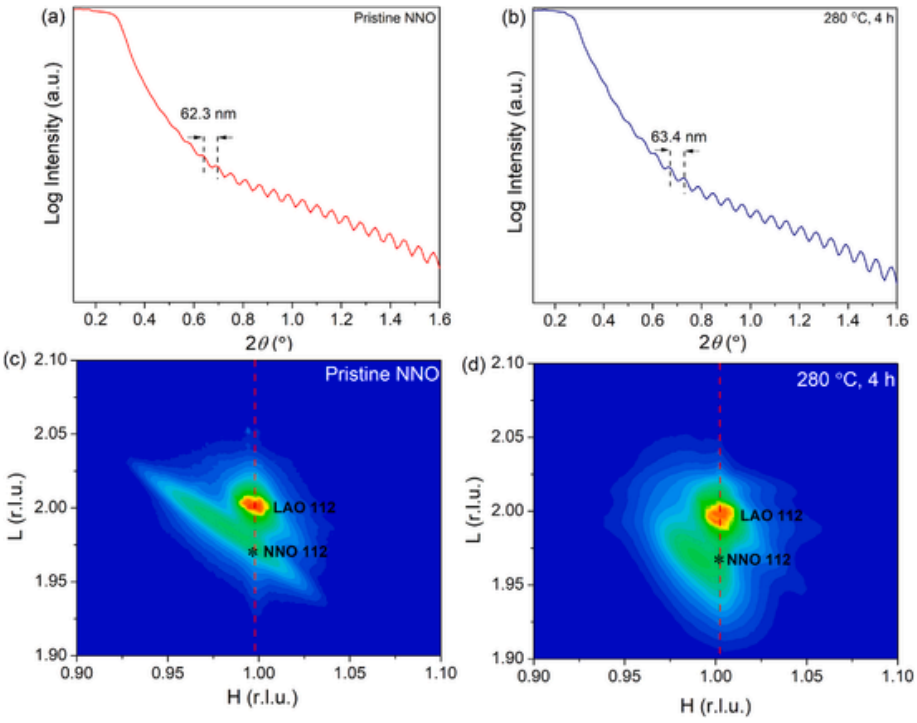

Fig. 3. (a) Synchrotron X-ray reflectivity (XRR) patterns of (a) pristine NNO and (b) NNO thin film annealed at 280 °C for 4 h with CaH_2. Film thickness values of 62.3 and 63.4 nm were extracted from the thickness fringes of XRR curves in (a) and (b), respectively. Synchrotron X-ray reciprocal space mapping (RSM) collected around the (112) diffraction maximum of LAO for (c) pristine NNO and (d) NNO thin film annealed at 280 °C for 4 h with CaH_2. Pseudocubic lattice constant of LAO is used to define the reciprocal lattice unit (r.l.u). The epitaxial NNO strained in the (001) plane is indicated by (*). Dashed lines are used as guides-to-the-eye. The diagonal elongation of the RSM spot reveals that pristine NNO thin film is partially relaxed on the (001) surface of the LAO substrate. The degree of relaxation seems to decrease upon CaH_2 annealing.

only ~4300 Ω. Such a large difference in the modulation of room-temperature resistance invariably signifies the electron doping *via* hydrogen incorporation of NNO during to CaH_2 annealing process. While above experiments and the results from Raman spectroscopy support hydrogen doping of NNO thin films, formation of oxygen vacancies during CaH_2 annealing cannot be excluded. It has been reported that CaH_2 can act as an oxygen getter creating highly reducing conditions, which facilitates the formation of reduced oxides [27]. In order to qualitatively probe the formation of oxygen vacancies and its impact on resistivity modulation, we have performed re-annealing of CaH_2 annealed NNO samples in air and collected I–V data. As shown in ESI-Fig. 5, the resistance of the sample annealed with CaH_2 at 280 °C for 3 h (~88600) could be lowered to ~30000 Ω by re-annealing at 200 °C for 3 h in air. This observation may indicate the possible deintercalation of H^+ from the interstitial sites of the NNO lattice. As mentioned earlier, similar lowering of the room-temperature resistance upon re-annealing in air was observed for the H–NNO thin films, which were obtained after hydrogen doping in 5% H_2/95% Ar forming gas at 125 °C. It should be mentioned that the binding strength of H^+ to the NNO lattice might be different in CaH_2 annealed samples in comparison to that of the samples annealed in forming gas. This may be evident from the longer annealing time (3–6 h) required for hydrogen deintercalation in the former case compared to the latter (15 min) at 200 °C. Noticeably, prolonged re-annealing for 12 h in air was required to recover the room-temperature resistance of pristine NNO revealing the existence of oxygen vacancies in CaH_2 annealed samples. Therefore, it may be inferred that the modulation of resistivity in H–NNO thin films is a combined effect of electron doping by interstitial hydrogen and oxygen vacancies. However, as revealed by our structural analysis and electrical property measurements, it is likely hydrogen doping is the dominant mechanism behind the resistivity modulation of H–NNO thin films (*vide infra*) obtained from CaH_2 annealing under the annealing conditions reported in this study.

Synchrotron X-ray structure analysis was performed to further understand the impact of CaH_2 annealing on NNO thin films. To this end, synchrotron XRD, XRR, and RSM data were collected on representative pristine NNO and H–NNO (4h). Findings from this analysis are summarized in Fig. 3 and ESI-Fig. 6. The shift of the (002) diffraction maximum of NNO to lower L values upon CaH_2 annealing supports the lattice expansion due to hydrogen doping (ESI-Fig. 6). Periodic oscillations (thickness fringes) of the XRR curves were used to determine the film thickness before and after CaH_2 annealing. The estimated thickness values were 62.3 and 63.4 nm, respectively for pristine NNO and H–NNO (4h) thin films (Fig. 3a and b). Thus, a minimal change in the thickness of NNO thin film was caused by CaH_2 annealing at 280 °C for 4 h, which may be attributed to the hydrogen intercalation into NNO thin film. In addition, the amplitudes of the oscillations of the XRR curves of both samples remained almost the same suggesting that surface roughness of NNO thin film was not significantly altered during the CaH_2 annealing process. Reciprocal space mapping was performed around the (112) Bragg reflection of LAO (reciprocal space coordinates (H, K, L), where K = 1) for pristine NNO and H–NNO (4h) thin films (Fig. 3c and d). The diagonal elongation of the RSM spot revealed that pristine NNO thin film is not fully strained on the (001) surface of the LAO substrate. However, the degree of relaxation seems to be lowered upon CaH_2 annealing as evident from the reduced diagonal elongation observed in the RSM spot of H–NNO (4h) thin film.

Next, we focused on establishing the effect of CaH_2 annealing on the oxidation state of Ni in H–NNO using XPS analysis. Results from this analysis are shown in Fig. 4. The description of the oxidation state of a Ni species using a single peak in XPS is prohibited by the effects of multiplet splitting and electronic screening [36,37]. However, Ni $2p_{3/2}$ core-level peak of pristine NNO located at ~854.5 eV gradually shifts to ~853.9 eV in H–NNO upon CaH_2 annealing for 4 h (Fig. 4a and b). This indicated the reduction of oxidation state of Ni towards Ni^{2+} due to hydrogen incorporation by CaH_2 annealing. A significant change in the

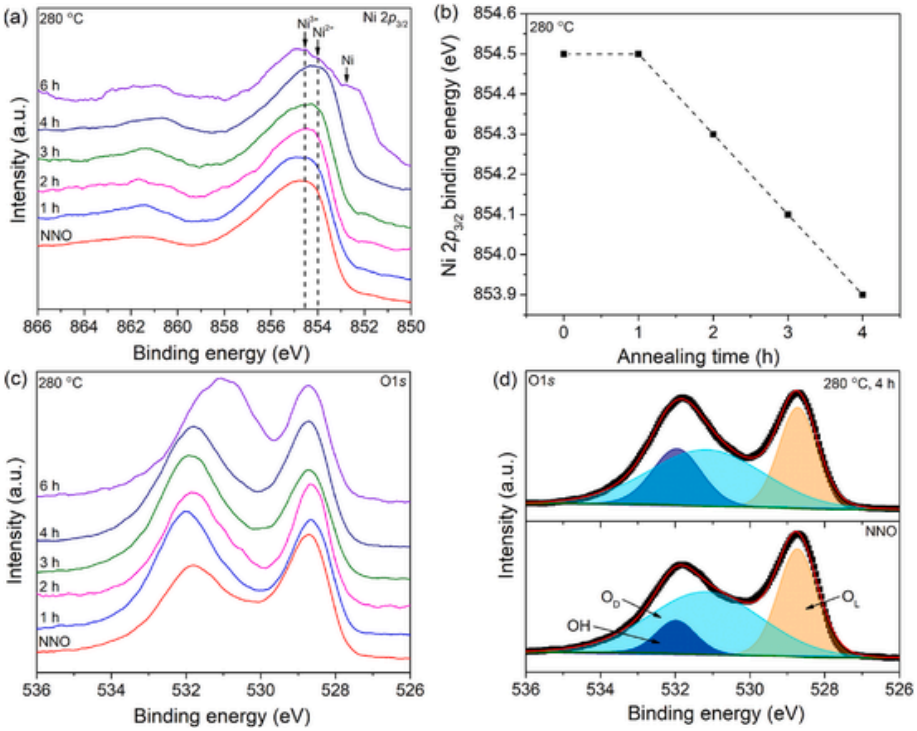

Fig. 4. (a) Ni $2p_{3/2}$ XPS spectra of pristine NNO and NNO samples annealed with CaH_2 at 280 °C for 1–6 h. The shift of the maximum of Ni $2p_{3/2}$ XPS peak to lower binding energies with increasing annealing time corresponds to the reduction of the oxidation state of Ni towards +2 upon electron doping. Arrows indicate the Ni $2p_{3/2}$ binding energies for Ni^{3+}, Ni^{2+}, and Ni. Dashed lines are used as guides-to-the-eye. (b) The plot of the maximum of Ni $2p_{3/2}$ binding energy vs. CaH_2 annealing time. (c) O 1*s* XPS spectra of pristine NNO and NNO samples annealed with CaH_2 at 280 °C for 1–6 h. (d) Representative O 1*s* XPS spectra of pristine NNO (bottom) and H–NNO (4 h) (top) could be fit with three peaks to account for the contributions from lattice oxygen (O_L, orange), oxygen defects (O_D, cyan), and hydroxyl groups (OH, blue).

shape of the Ni $2p_{3/2}$ peak is observed in the XPS spectrum collected after CaH_2 annealing for 6 h. Noticeably, an additional shoulder at ~852.7 eV is detected, which indicates the formation of metallic Ni due to prolonged CaH_2 annealing [38]. This is consistent with the degradation of NNO thin films upon CaH_2 annealing as revealed by XRD. In contrast, hydrogenation by CaH_2 annealing seemed to have no significant effect on the position and shape Nd $3d_{5/2}$ peak implying oxidation state of Nd remains unchanged at +3. Fig. 4c shows the evolution of O 1*s* XPS spectra of NNO and H–NNO thin films. The intensity of the XPS peak maximum located at ~532 eV increased compared to that of the ~529 eV with increasing annealing time. To gain further insight on this behavior, XPS spectra of pristine NNO and H–NNO (4h) thin films were fitted using three peaks centered at ~528.7, 531.2, and 532.0 corresponding to contributions from lattice oxygen (O_L, orange), oxygen defects (O_D, cyan), and hydroxyl groups (OH, blue), respectively (Fig. 4d) [39,40]. The peak area corresponding to OH groups increased with CaH_2 annealing of thin films for 4 h at 280 °C.

Findings from the XPS analysis on the effect of Ni valence state in NNO thin films by CaH_2 annealing were in good agreement with the results from XAS. Analysis of Ni *L* and O *K* edge X-ray absorption spectra of NNO and selected H–NNO samples are summarized in Fig. 5. Upon CaH_2 annealing, (1) the peak positions of Ni L_2 and L_3 edges shifts to lower energies; this was more pronounced in the case of Ni L_2 and (2) the spectral weight of the high-energy shoulder of Ni L_3 spectra decreased (Fig. 5a). These observations revealed the reduction of the oxidation state of Ni towards +2 with hydrogen incorporation. The Ni L_3 spectra were quantitatively assessed by fitting with two Gaussian components centered at ~855 (Ni^{3+}) and ~853.8 eV (Ni^{2+}) after subtracting a linear background [41]. As shown in Fig. 5b and c, the peak area of the high-energy contribution is suppressed due to CaH_2 annealing. As a result, the ratio of the peak areas centered at ~855 (Ni^{3+}) and ~853.8 eV (Ni^{2+}) decreases with increasing CaH_2 annealing time. Therefore, XAS analysis demonstrates the dominance of divalent Ni in H–NNO thin films, which is a consequence of the injection of the doped electrons by CaH_2 annealing to the conduction band of Ni in pristine NNO thin films. On the other hand, inspection of the O *K* edge spectra revealed a gradual suppression of the pre-edge peak located at ~529 eV upon electron doping by CaH_2 annealing. This pre-edge feature represents the electronic transition from O 1*s* core level to the ligand hole *L* in the $3d^{7+\delta}L^{\delta}$ configuration of Ni [42]. Therefore, the suppression of this pre-edge feature indicates the electron filling of Ni 3*d*–O 2*p* hybridized orbitals upon CaH_2 annealing.

We then measured the temperature-dependent electrical transport properties of pristine NNO and H–NNO thin films. Results from these studies are depicted in Fig. 6. Pristine NNO shows the intrinsic MIT in the resistivity (ρ) vs. temperature (T) plot shown in Fig. 6a. A substantial increase in the resistivity of NNO thin films could be achieved by CaH_2 annealing at 280 °C for 2–4 h. In fact, a resistivity enhancement of ~4 orders magnitude larger than the resistivity of pristine NNO was realized for the H–NNO (4 h) sample at 300 K (Fig. 6b and c). In order to understand the carrier transport mechanisms of NNO and H–NNO films, we performed further quantitative analysis of temperature-dependent resistivity data. Variable range hopping model (VRH) given by $\rho(T) = \rho_1 \exp(T_0/T)^p$ can be used to describe the low-temperature transport mechanism of rare-earth nickelates [12,33,43]. Here, $\rho(T)$ is the resistivity at temperature T K, ρ_1 is the prefactor, T_0 is the characteristic temperature, and p is the exponent related to the conduction mechanism; $p = 1/4$ for Mott VRH mechanism. The linearity of ln ($\rho(T)$) vs. $T^{-0.25}$ indicated that low-temperature transport of NNO and H–NNO thin films displays the Mott VRH mechanism. The extracted carrier localization lengths are plotted as a function of the annealing time in Fig. 6d. The drop of the localization length from ~98.4 (NNO) to 2.3 nm H–NNO (4 h) signifies that the electrons are strongly localized

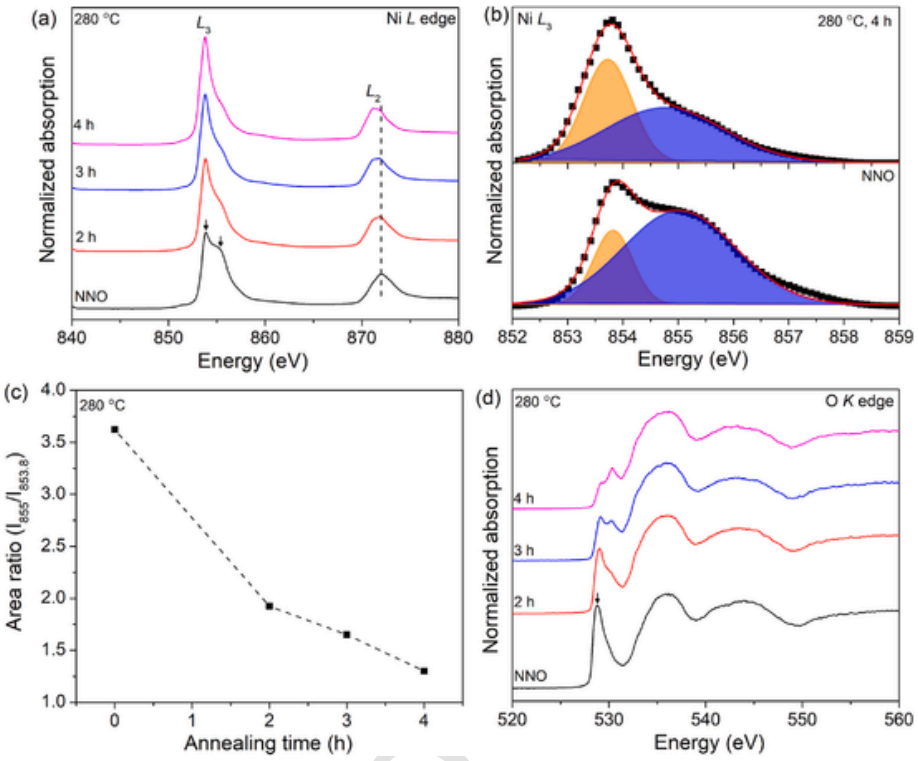

Fig. 5. (a) Normalized Ni *L* edge XAS spectra of pristine NNO and selected NNO samples annealed with CaH_2 at 280 °C for 2–4 h. Arrows indicate the components of XAS spectra related to Ni^{2+} (low-energy) and Ni^{3+} (high-energy). The spectral weight of the high-energy component of Ni L_3 spectra decreased upon CaH_2 annealing suggesting a decrease of the oxidation state of Ni. This argument is further supported by the shift of the maximum of Ni L_2 spectra to lower energies with increasing annealing time. (b) Ni L_3 edge XAS were fit using two Gaussian components centered at ~855 (blue) and ~853.8 eV (orange) after subtracting a linear background. (c) The area ratio of the two Gaussian components ($I_{855}/I_{853.8}$) decreases as a function of annealing time revealing the reduction of Ni^{3+}. Dashed lines in (a) and (c) are used as guides-to-the-eye. (d) The evolution of O *K* edge spectra with increasing durations of CaH_2 annealing. The gradual suppression of the pre-edge peak located at ~529 eV (shown by an arrow) of O *K* edge spectra indicates the electron filling of Ni 3*d*–O 2*p* hybridized orbitals upon CaH_2 annealing.

in CaH_2 annealed samples. This is in line with the large modulation of electrical resistivity upon electron doping by CaH_2 annealing.

Overall, the findings of our study highlight the potential of using CaH_2 as an *in-situ* low temperature hydrogen source to carry out electron doping of NNO thin films. In particular, the feasibility of incorporating hydrogen into NNO thin films, which are physically separated from CaH_2 reduces the number of cleaning steps required after annealing. Previously, Kobayashi and coworkers demonstrated the feasibility of utilizing gas phase topochemical reduction reactions to synthesize oxygen deficient metastable transition metal oxides using CaH_2 as the reductant [27]. They also reported the physically separated reduction of $SrFeO_{2.5}$ and $LaNiO_3$ thin films by CaH_2 annealing to yield $SrFeO_2$ and $LaNiO_2$, respectively; an Al foil was employed as the spacer between the thin film and CaH_2 pellet. The reduction of the transition metal oxides occurred due to the H_2 gas, which was *in-situ* generated by the chemical reactions between CaH_2/metal oxide and CaH_2/$Ca(OH)_2$ impurity [27,28]. Similarly, here, CaH_2 annealing at 280 °C is expected to generate *in-situ* H_2, which would be incorporated into the crystal structure of NNO thin films. We emphasize that the stabilization of H–NNO on LAO in our case and the formation of $NdNiO_2$ and/or $NdNiO_xH_y$ on STO in previous studies upon CaH_2 annealing of NNO thin films may also be ascribed to the difference between the strain introduced by the two substrates [17,23,35]. STO is expected to exert a larger tensile strain on NNO thin films compared to the smaller compressive strain applied by LAO [30]. Previous theoretical and experimental studies have also emphasized higher reactivity of thin films compared to bulk powders, as well as epitaxial strain, and the cation composition of the thin film (i.e., the type RE) as factors affecting hydrogen incorporation into rare-earth nickelate and other perovskite thin films [44–46]. A systematic study of steric effects on kinetics of hydrogen incorporation would make a subject of future study.

4. Conclusions

In conclusion, we have demonstrated the feasibility of exploiting CaH_2 annealing as an electron doping strategy to tune the electrical resistivity of $NdNiO_3$ thin films. CaH_2 annealing was performed in a specially designed glass ampule with two interconnected chambers. XRD and Raman spectroscopy indicated the electron doping into NNO lattice without inducing the formation of any impurities by CaH_2 annealing at 280 °C for 1–4 h. Simultaneously, as revealed by XPS and XAS, hydrogen incorporation accompanied with a change in the oxidation state of Ni towards +2 caused by electron doping of NiO_6 octahedra. This led to a strong localization of electrons and resulted in ~4 orders of magnitude enhancement of room temperature resistivity of H–NNO thin films. The findings underscore the broad applicability of CaH_2 annealing as a synthetic method to manipulate the electrical properties of correlated oxides by changing the interstitial defect density and cation valence states.

CRediT authorship contribution statement

Dinesh K. Amarasinghe : Investigation, Methodology, Writing – original draft. **Haoming Yu :** Investigation, Methodology, Writing – original draft. **Fanny Rodolakis :** Writing – review & editing. **Hua Zhou :** Writing – review & editing. **Hui Cao :** Writing – review & editing. **Shriram Ramanathan :** Conceptualization, Resources, Writing – review & editing, Funding acquisition.

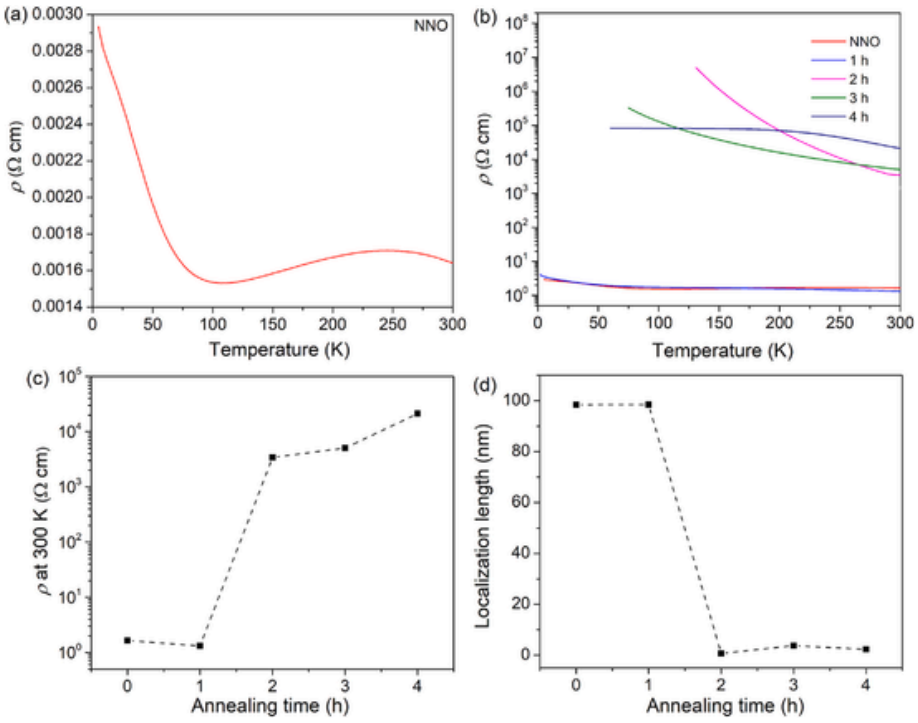

Fig. 6. (a) The plot of resistivity (ρ) vs. temperature (T) of pristine NNO thin film upon cooling from 300 to 2 K. (b) Temperature-dependent resistivity data of pristine NNO and NNO thin films annealed at 280 ˚C for 1, 2, 3, and 4 h with CaH_2. (c) Electrical resistivity of NNO and H–NNO at 300 K as a function of CaH_2 annealing time. ~ 4 orders of increase in the magnitude of ressistivity at 300 K is achieved, which is attributed to the strong localization of electrons. (d) Localization lengths extracted from fitting the low-temperature resistivity data of NNO and H–NNO thin films to Mott VRH model. A significant drop in the localization lengths was noticed in H–NNO films in agreement with the large modulation of electrical resistivity. Dashed lines in (c) and (d) are used as guides-to-the-eye.

Declaration of competing interest

The authors declare that they have no known competing financial interests or personal relationships that could have appeared to influence the work reported in this paper.

Data availability

Data will be made available on request.

Acknowledgements

The authors would like to thank Jordan Smith, Scientific Glass Blower of the Department of Chemistry at Purdue University for technical assistance with designing and sealing the encapsulation vessels and adapters for the CaH_2 annealing experiments. We acknowledge NSF Award No. 1904081 for support.The extreme environment annealing experiments were supported in part by Air Force Office of Scientific Research grant (AFOSR) FA9550-18-1-0250. The synchrotron XRD measurements were carried out at Advanced Photon Source, a U.S. Department of Energy (DOE) Office of Science User Facility, operated for the DOE Office of Science by Argonne National Laboratory under Contract No. DE-AC02-06CH11357.

Supporting information

The following Supporting Information is provided:

(1) (a) XRD patterns and (b) Raman spectra of (i) bare LAO substrate, (ii) NNO thin film on LAO, (iii) NNO thin film vacuum annealed without CaH_2 at 280 ˚C for 3 h, (iv) NNO thin film annealed with CaH_2 at 280 ˚C for 3 h, (v) NNO thin film annealed with 5% H_2/95% Ar forming gas at 125 ˚C for 10 min, and (vi) NNO thin film annealed with CaH_2 at 280 ˚C for 3 h after patterning Pt electrodes.
(2) Plot of out-of-plane lattice constant of NNO thin film vs. CaH_2 annealing time.
(3) (a) XRD patterns of LAO substrate, NNO thin film, NNO thin film annealed with CaH_2 at 280 ˚C for 6 h, and re-annealed at 500 ˚C for 24 h. (b) XRD patterns of LAO substrate, NNO thin film, NNO thin film annealed with CaH_2 at 280 ˚C for 12 h, and re-annealed at 500 ˚C for 24 h.
(4) (a) Room-temperature I–V curves for pristine NNO, NNO thin film annealed with 5% H_2/95% Ar forming gas at 125 ˚C for 10 min with Pt electrodes, and NNO thin film annealed with CaH_2 at 280 ˚C for 3 h with Pt electrodes (b) Room-temperature I–V curves for pristine NNO, NNO thin film annealed with 5% H_2/95% Ar forming gas at 125 ˚C for 10 min with no Pt electrodes, NNO thin film annealed with 5% H_2/95% Ar forming gas at 125 ˚C for 10 min with Pt electrodes, NNO thin film annealed with 5% H_2/95% Ar forming gas at 125 ˚C for 10 min with Pt electrodes followed by re-annealing in air at 200 ˚C for 15 min, NNO thin film vacuum annealed without CaH_2 at 280 ˚C for 3 h, and NNO thin film annealed with CaH_2 at 280 ˚C for 3 h.

(5) Room-temperature I–V curves for pristine NNO, NNO thin film annealed with CaH_2 at 280 °C for 3 h, NNO thin film annealed with CaH_2 at 280 °C for 3 h followed by re-annealing in air at 100 °C for 1 h, and NNO thin films annealed with CaH_2 at 280 °C for 3 h followed by re-annealing in air at 200 °C for 3, 6, and 12 h.
(6) (a) Synchrotron XRD patterns of NNO thin film and NNO thin film annealed with CaH_2 at 280 °C for 4 h.

Appendix A. Supplementary data

Supplementary data to this article can be found online at https://doi.org/10.1016/j.jssc.2022.123512.

References

[1] J.B. Torrance, P. Lacorre, A.I. Nazzal, E.J. Ansaldo, C. Niedermayer, Systematic study of insulator-metal transitions in perovskites $RNiO_3$ (R = Pr, Nd, Sm, Eu) due to closing of charge-transfer gap, Phys. Rev. B 45 (14) (1992) 8209–8212, https://doi.org/10.1103/PhysRevB.45.8209.

[2] S. Catalano, M. Gibert, J. Fowlie, J. Íñiguez, J.M. Triscone, J. Kreisel, Rare-earth nickelates $RNiO_3$: thin films and heterostructures, Rep. Prog. Phys. 81 (4) (2018) 046501, https://doi.org/10.1088/1361-6633/aaa37a.

[3] S. Middey, J. Chakhalian, P. Mahadevan, J.W. Freeland, A.J. Millis, D.D. Sarma, Physics of ultrathin films and heterostructures of rare-earth nickelates, Annu. Rev. Mater. Res. 46 (1) (2016) 305–334, https://doi.org/10.1146/annurev-matsci-070115-032057.

[4] C. Oh, S. Heo, H.M. Jang, J. Son, Correlated memory resistor in epitaxial $NdNiO_3$ heterostructures with asymmetrical proton concentration, Appl. Phys. Lett. 108 (12) (2016) 122106, https://doi.org/10.1063/1.4944842.

[5] J. Shi, Y. Zhou, S. Ramanathan, Colossal resistance switching and band gap modulation in a perovskite nickelate by electron doping, Nat. Commun. 5 (1) (2014) 4860, https://doi.org/10.1038/ncomms5860.

[6] H.-T. Zhang, T.J. Park, A.N.M.N. Islam, D.S.J. Tran, S. Manna, Q. Wang, S. Mondal, H. Yu, S. Banik, S. Cheng, H. Zhou, S. Gamage, S. Mahapatra, Y. Zhu, Y. Abate, N. Jiang, S.K.R.S. Sankaranarayanan, A. Sengupta, C. Teuscher, S. Ramanathan, Reconfigurable perovskite nickelate electronics for artificial intelligence, Science 375 (6580) (2022) 533–539, https://doi.org/10.1126/science.abj7943.

[7] G.H. Aydogdu, S.D. Ha, B. Viswanath, S. Ramanathan, Epitaxy, strain, and composition effects on metal–insulator transition characteristics of $SmNiO_3$ thin films, J. Appl. Phys. 109 (12) (2011) 124110, https://doi.org/10.1063/1.3598055.

[8] J. Chen, W. Mao, L. Gao, F. Yan, T. Yajima, N. Chen, Z. Chen, H. Dong, B. Ge, P. Zhang, X. Cao, M. Wilde, Y. Jiang, T. Terai, J. Shi, Electron-doping mottronics in strongly correlated perovskite, Adv. Mater. 32 (6) (2020) 1905060, https://doi.org/10.1002/adma.201905060.

[9] J. Li, S. Ramanathan, R. Comin, Carrier doping physics of rare earth perovskite nickelates $RENiO_3$, Front. Phy. 10 (2022), https://doi.org/10.3389/fphy.2022.834882.

[10] Y. Sun, M. Kotiuga, D. Lim, B. Narayanan, M. Cherukara, Z. Zhang, Y. Dong, R. Kou, C.-J. Sun, Q. Lu, I. Waluyo, A. Hunt, H. Tanaka, N. Hattori Azusa, S. Gamage, Y. Abate, G. Pol Vilas, H. Zhou, K.R.S. Sankaranarayanan Subramanian, B. Yildiz, M. Rabe Karin, S. Ramanathan, Strongly correlated perovskite lithium ion shuttles, Proc. Natl. Acad. Sci. USA 115 (39) (2018) 9672–9677, https://doi.org/10.1073/pnas.1805029115.

[11] T. Onozuka, A. Chikamatsu, T. Katayama, Y. Hirose, I. Harayama, D. Sekiba, E. Ikenaga, M. Minohara, H. Kumigashira, T. Hasegawa, Reversible changes in resistance of perovskite nickelate $NdNiO_3$ thin films induced by fluorine substitution, ACS Appl. Mater. Interfaces 9 (12) (2017) 10882–10887, https://doi.org/10.1021/acsami.7b00855.

[12] M. Kotiuga, Z. Zhang, J. Li, F. Rodolakis, H. Zhou, R. Sutarto, F. He, Q. Wang, Y. Sun, Y. Wang, A. Aghamiri Neda, B. Hancock Steven, P. Rokhinson Leonid, P. Landau David, Y. Abate, W. Freeland John, R. Comin, S. Ramanathan, M. Rabe Karin, Carrier localization in perovskite nickelates from oxygen vacancies, Proc. Natl. Acad. Sci. USA 116 (44) (2019) 21992–21997, https://doi.org/10.1073/pnas.1910490116.

[13] L. Wang, S. Dash, L. Chang, L. You, Y. Feng, X. He, K.-j. Jin, Y. Zhou, H.G. Ong, P. Ren, S. Wang, L. Chen, J. Wang, Oxygen vacancy induced room-temperature metal–insulator transition in nickelate films and its potential application in photovoltaics, ACS Appl. Mater. Interfaces 8 (15) (2016) 9769–9776, https://doi.org/10.1021/acsami.6b00650.

[14] T. Yamanaka, A.N. Hattori, L.N. Pamasi, S. Takemoto, K. Hattori, H. Daimon, K. Sato, H. Tanaka, Effects of off-stoichiometry in the epitaxial $NdNiO_3$ film on the suppression of its metal-insulator-transition properties, ACS Appl. Electr. Mater. 1 (12) (2019) 2678–2683, https://doi.org/10.1021/acsaelm.9b00662.

[15] T. Orvis, M. Surendran, Y. Liu, S. Niu, S. Muramoto, A.J. Grutter, J. Ravichandran, Electron doping $BaZrO_3$ via topochemical reduction, ACS Appl. Mater. Interfaces 11 (24) (2019) 21720–21726, https://doi.org/10.1021/acsami.9b06370.

[16] M.A. Hayward, M.J. Rosseinsky, Cool conditions for mobile ions, Nature 450 (7172) (2007) 960–961, https://doi.org/10.1038/450960a.

[17] D. Li, K. Lee, B.Y. Wang, M. Osada, S. Crossley, H.R. Lee, Y. Cui, Y. Hikita, H.Y. Hwang, Superconductivity in an infinite-layer nickelate, Nature 572 (7771) (2019) 624–627, https://doi.org/10.1038/s41586-019-1496-5.

[18] M. Osada, B.Y. Wang, B.H. Goodge, K. Lee, H. Yoon, K. Sakuma, D. Li, M. Miura, L.F. Kourkoutis, H.Y. Hwang, A Superconducting praseodymium nickelate with infinite layer structure, Nano Lett. 20 (8) (2020) 5735–5740, https://doi.org/10.1021/acs.nanolett.0c01392.

[19] T. Katayama, A. Chikamatsu, K. Yamada, K. Shigematsu, T. Onozuka, M. Minohara, H. Kumigashira, E. Ikenaga, T. Hasegawa, Epitaxial growth and electronic structure of oxyhydride $SrVO_2H$ thin films, J. Appl. Phys. 120 (8) (2016) 085305, https://doi.org/10.1063/1.4961446.

[20] G. Bouilly, T. Yajima, T. Terashima, Y. Kususe, K. Fujita, C. Tassel, T. Yamamoto, K. Tanaka, Y. Kobayashi, H. Kageyama, Substrate-induced anion rearrangement in epitaxial thin films of $LaSrCoO_{4-x}H_x$, CrystEngComm 16 (41) (2014) 9669–9674, https://doi.org/10.1039/C4CE01268B.

[21] T. Katayama, A. Chikamatsu, H. Kamisaka, Y. Yokoyama, Y. Hirata, H. Wadati, T. Fukumura, T. Hasegawa, Topotactic synthesis of strontium cobalt oxyhydride thin film with perovskite structure, AIP Adv. 5 (10) (2015) 107147, https://doi.org/10.1063/1.4935190.

[22] T. Yajima, A. Kitada, Y. Kobayashi, T. Sakaguchi, G. Bouilly, S. Kasahara, T. Terashima, M. Takano, H. Kageyama, Epitaxial thin films of $ATiO_{3-x}H_x$ (A = Ba, Sr, Ca) with metallic conductivity, J. Am. Chem. Soc. 134 (21) (2012) 8782–8785, https://doi.org/10.1021/ja302465c.

[23] T. Onozuka, A. Chikamatsu, T. Katayama, T. Fukumura, T. Hasegawa, Formation of defect-fluorite structured $NdNiO_xH_y$ epitaxial thin films via a soft chemical route from $NdNiO_3$ precursors, Dalton Trans. 45 (30) (2016) 12114–12118, https://doi.org/10.1039/C6DT01737A.

[24] L. Si, W. Xiao, J. Kaufmann, J.M. Tomczak, Y. Lu, Z. Zhong, K. Held, Topotactic hydrogen in nickelate superconductors and akin infinite-layer oxides ABO_2, Phys. Rev. Lett. 124 (16) (2020) 166402, https://doi.org/10.1103/PhysRevLett.124.166402.

[25] O.I. Malyi, J. Varignon, A. Zunger, Bulk $NdNiO_2$ is thermodynamically unstable with respect to decomposition while hydrogenation reduces the instability and transforms it from metal to insulator, Phys. Rev. B 105 (1) (2022) 014106, https://doi.org/10.1103/PhysRevB.105.014106.

[26] S. Balakrishnan, M.V. Sofianos, M. Paskevicius, M.R. Rowles, C.E. Buckley, Destabilized calcium hydride as a promising high-temperature thermal battery, J. Phys. Chem. C 124 (32) (2020) 17512–17519, https://doi.org/10.1021/acs.jpcc.0c04754.

[27] Y. Kobayashi, Z. Li, K. Hirai, C. Tassel, F. Loyer, N. Ichikawa, N. Abe, T. Yamamoto, Y. Shimakawa, K. Yoshimura, M. Takano, O.J. Hernandez, H. Kageyama, Gas phase contributions to topochemical hydride reduction reactions, J. Solid State Chem. 207 (2013) 190–193, https://doi.org/10.1016/j.jssc.2013.09.006.

[28] A. Ikeda, T. Manabe, M. Naito, Comparison of reduction agents in the synthesis of infinite-layer $LaNiO_2$ films, Phys. C: Superconduct. Appl. 506 (2014) 83–86, https://doi.org/10.1016/j.physc.2014.09.002.

[29] J.F. De Natale, P.H. Kobrin, Lattice distortion effects on electrical switching in epitaxial thin film $NdNiO_3$, J. Mater. Res. 10 (12) (1995) 2992–2995, https://doi.org/10.1557/JMR.1995.2992.

[30] J. Liu, M. Kareev, B. Gray, J.W. Kim, P. Ryan, B. Dabrowski, J.W. Freeland, J. Chakhalian, Strain-mediated metal–insulator transition in epitaxial ultrathin films of $NdNiO_3$, Appl. Phys. Lett. 96 (23) (2010) 233110, https://doi.org/10.1063/1.3451462.

[31] Q. Wang, H. Zhou, S. Ramanathan, Electron doping-induced metal–insulator transition in $LaNiO_3$ and memory devices, ACS Appl. Electr. Mater. 4 (5) (2022) 2463–2472, https://doi.org/10.1021/acsaelm.2c00242.

[32] M. Zaghrioui, A. Bulou, P. Laffez, P. Lacorre, Raman study of metal–insulator transition in $NdNiO_3$ thin films, J. Magn. Magn Mater. 211 (1) (2000) 238–242, https://doi.org/10.1016/S0304-8853(99)00740-4.

[33] K. Ramadoss, N. Mandal, X. Dai, Z. Wan, Y. Zhou, L. Rokhinson, Y.P. Chen, J. Hu, S. Ramanathan, Sign reversal of magnetoresistance in a perovskite nickelate by electron doping, Phys. Rev. B 94 (23) (2016) 235124, https://doi.org/10.1103/PhysRevB.94.235124.

[34] Y. Sun, Q. Wang, T.J. Park, T.E. Gage, Z. Zhang, X. Wang, D. Zhang, X. Sun, J. He, H. Zhou, D.G. Lim, C. Huang, H. Yu, X. Chen, H. Wang, J. Mei, E. Deguns, S. Ramanathan, Electrochromic properties of perovskite $NdNiO_3$ thin films for smart windows, ACS Appl. Electr. Mater. 3 (4) (2021) 1719–1731, https://doi.org/10.1021/acsaelm.1c00030.

[35] K. Lee, B.H. Goodge, D. Li, M. Osada, B.Y. Wang, Y. Cui, L.F. Kourkoutis, H.Y. Hwang, Aspects of the synthesis of thin film superconducting infinite-layer nickelates, Apl. Mater. 8 (4) (2020) 041107, https://doi.org/10.1063/5.0005103.

[36] A.P. Grosvenor, M.C. Biesinger, R.S.C. Smart, N.S. McIntyre, New interpretations of XPS spectra of nickel metal and oxides, Surf. Sci. 600 (9) (2006) 1771–1779, https://doi.org/10.1016/j.susc.2006.01.041.

[37] H.W. Nesbitt, D. Legrand, G.M. Bancroft, Interpretation of Ni2p XPS spectra of Ni conductors and Ni insulators, Phys. Chem. Miner. 27 (5) (2000) 357–366, https://

doi.org/10.1007/s002690050265.
[38] A.F. Carley, S.D. Jackson, J.N. O'Shea, M.W. Roberts, The formation and characterisation of Ni^{3+}–an X-ray photoelectron spectroscopic investigation of potassium-doped Ni(110)–O, Surf. Sci. 440 (3) (1999) L868–L874, https://doi.org/10.1016/S0039-6028(99)00872-9.
[39] Z. Zhang, S. Mondal, S. Mandal, M. Allred Jason, A. Aghamiri Neda, A. Fali, Z. Zhang, H. Zhou, H. Cao, F. Rodolakis, L. McChesney Jessica, Q. Wang, Y. Sun, Y. Abate, K. Roy, M. Rabe Karin, S. Ramanathan, Neuromorphic learning with Mott insulator NiO, Proc. Natl. Acad. Sci. USA 118 (39) (2021) e2017239118, https://doi.org/10.1073/pnas.2017239118.
[40] S. Mickevičius, S. Grebinskij, V. Bondarenka, B. Vengalis, K. Šliužienė, B.A. Orlowski, V. Osinniy, W. Drube, Investigation of epitaxial $LaNiO_{3\,x}$ thin films by high-energy XPS, J. Alloys Compd. 423 (1) (2006) 107–111, https://doi.org/10.1016/j.jallcom.2005.12.038.
[41] M. Medarde, A. Fontaine, J.L. García-Muñoz, J. Rodríguez-Carvajal, M. de Santis, M. Sacchi, G. Rossi, P. Lacorre, $RNiO_3$ perovskites (R = Pr, Nd): nickel valence and the metal–insulator transition investigated by X-ray-absorption spectroscopy, Phys. Rev. B 46 (23) (1992) 14975–14984, https://doi.org/10.1103/PhysRevB.46.14975.
[42] J. Li, R.J. Green, Z. Zhang, R. Sutarto, J.T. Sadowski, Z. Zhu, G. Zhang, D. Zhou, Y. Sun, F. He, S. Ramanathan, R. Comin, Sudden collapse of magnetic order in oxygen-deficient nickelate films, Phys. Rev. Lett. 126 (18) (2021) 187602, https://doi.org/10.1103/PhysRevLett.126.187602.
[43] G. Catalan, R.M. Bowman, J.M. Gregg, Metal–insulator transitions in $NdNiO_3$ thin films, Phys. Rev. B 62 (12) (2000) 7892–7900, https://doi.org/10.1103/PhysRevB.62.7892.
[44] D. Kutsuzawa, Y. Hirose, A. Chikamatsu, S. Nakao, Y. Watahiki, I. Harayama, D. Sekiba, T. Hasegawa, Strain-enhanced topotactic hydrogen substitution for oxygen in $SrTiO_3$ epitaxial thin film, Appl. Phys. Lett. 113 (25) (2018) 253104, https://doi.org/10.1063/1.5057370.
[45] F. Bernardini, L. Iglesias, M. Bibes, A. Cano, Thin-film aspects of superconducting nickelates, Front. Phy. 10 (2022), https://doi.org/10.3389/fphy.2022.828007.
[46] H. Takatsu, M. Ochi, M. Namba, H. Li, A. Daniel, T. Terashima, K. Kuroki, H. Kageyama, Strain-assisted topochemical synthesis of La-doped $SrVO_2H$ films, Cryst. Growth Des. 21 (7) (2021) 3779–3785, https://doi.org/10.1021/acs.cgd.1c00098.

Supporting Information

Electron Doping of $NdNiO_3$ Thin Films Using Dual Chamber CaH_2 Annealing

Dinesh K. Amarasinghe,[1] Haoming Yu,[1] Fanny Rodolakis,[2] Hua Zhou,[2] Hui Cao,[3] and Shriram Ramanathan[1]*

[1]School of Materials Engineering, Purdue University, West Lafayette, IN 47907, USA

[2]X-ray Science Division, Advanced Photon Source, Argonne National Laboratory, Lemont, IL 60439, USA

[3]Materials Science Division, Argonne National Laboratory, Lemont, IL 60439, USA

*Corresponding Author. Email: shriram@purdue.edu

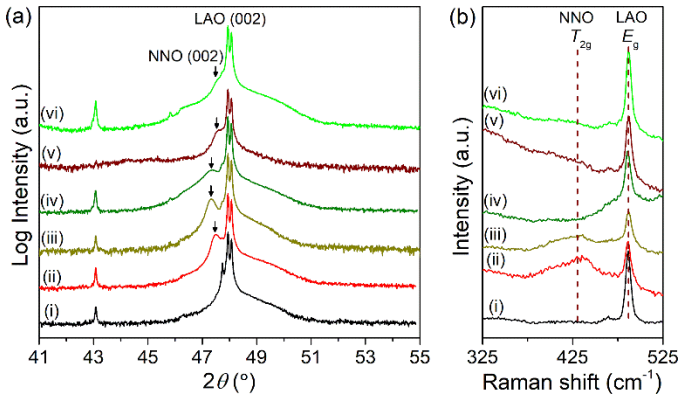

Fig. 1. (a) XRD patterns and (b) Raman spectra of (i) bare LAO substrate, (ii) NNO thin film on LAO, (iii) NNO thin film vacuum annealed without CaH_2 at 280 °C for 3 h, (iv) NNO thin film annealed with CaH_2 at 280 °C for 3 h, (v) NNO thin film annealed with 5% H_2/95% Ar forming gas at 125 °C for 10 minutes after patterning Pt electrodes, and (vi) NNO thin film annealed with CaH_2 at 280 °C for 3 h after patterning Pt electrodes. (002) reflection of LAO is labeled in (a). (002) reflection of NNO is labeled with pseudocubic notation and indicated by an arrow in (a). Dashed lines in (b) denote the Raman peak maxima of LAO and NNO located at ~487 and 433 cm^{-1}, respectively. The intensity of the T_{2g} Raman mode of NNO (at ~433 cm^{-1}) is not significantly changed by vacuum annealing without CaH_2 at 280 °C for 3 h. In contrast, this peak has disappeared in the case of NNO thin film annealed with CaH_2 at 280 °C for 3 h and NNO thin film annealed with 5% H_2/95% Ar forming gas at 125 °C for 10 minutes. Thus, the incorporation of in-situ generated hydrogen is the primary origin behind the resistivity modulation of NNO thin films.

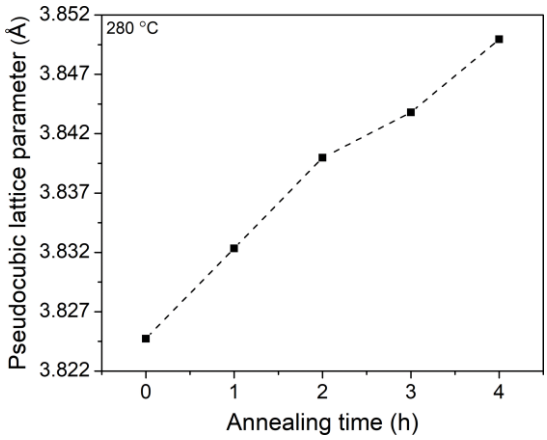

Fig. 2. The plot of out-of-plane lattice constant of NNO thin film vs. CaH_2 annealing time. An expansion of the out-of-plane lattice constant due to the strain induced by hydrogen doping is noticed upon CaH_2 annealing. Dashed lines are used as guides-to-the-eye.

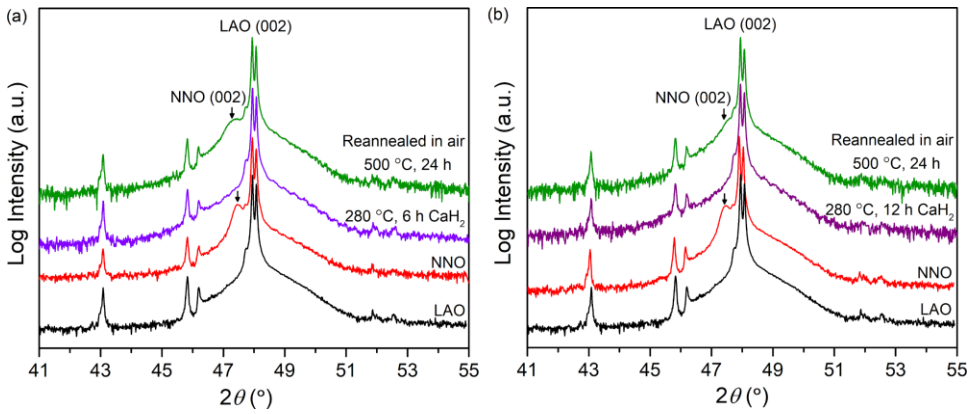

Fig. 3. (a) XRD patterns of LAO substrate, NNO thin film, NNO thin film annealed with CaH_2 at 280 °C for 6 h, and re-annealed at 500 °C for 24 h. (b) XRD patterns of LAO substrate, NNO thin film, NNO thin film annealed with CaH_2 at 280 °C for 12 h, and re-annealed at 500 °C for 24 h. (002) reflection of LAO is labeled. (002) reflection of NNO is labeled with pseudocubic notation and indicated by an arrow. CaH_2 annealing of NNO thin films at 280 °C for 6 and 12 h led to their decomposition as observed by the diminished intensity of the corresponding (002) diffraction maximum. Reappearance of this diffraction maximum upon re-annealing the films at 500 °C for 24 h in air indicated the recovery of the perovskite NNO structure.

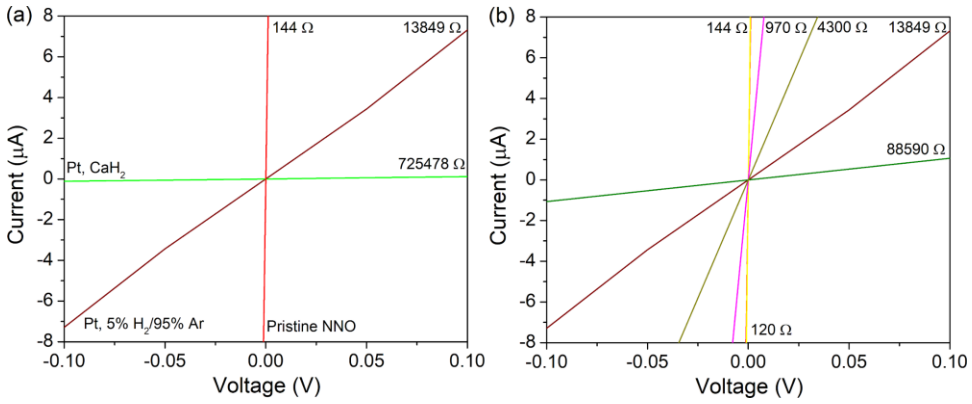

Fig. 4. (a) Room-temperature I-V curves for pristine NNO, NNO thin film annealed with 5% H_2/95% Ar forming gas at 125 °C for 10 minutes with Pt electrodes, and NNO thin film annealed with CaH_2 at 280 °C for 3 h with Pt electrodes (b) Room-temperature I-V curves for pristine NNO (red), NNO thin film annealed with 5% H_2/95% Ar forming gas at 125 °C for 10 minutes with no Pt electrodes (magenta), NNO thin film annealed with 5% H_2/95% Ar forming gas at 125 °C for 10 minutes with Pt electrodes (wine), NNO thin film annealed with 5% H_2/95% Ar forming gas at 125 °C for 10 minutes with Pt electrodes followed by re-annealing in air at 200 °C for 15 minutes (yellow), NNO thin film vacuum annealed without CaH_2 at 280 °C for 3 h (dark yellow), and NNO thin film annealed with CaH_2 at 280 °C for 3 h (olive). The corresponding room-temperature resistance of the thin films are provided next to the I-V trace.

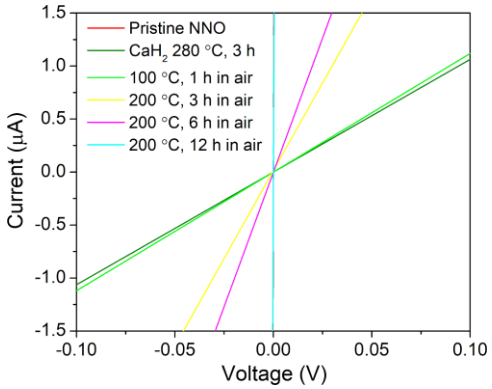

Fig. 5. Room-temperature I-V curves for pristine NNO (144 Ω), NNO thin film annealed with CaH_2 at 280 °C for 3 h (88590 Ω), NNO thin film annealed with CaH_2 at 280 °C for 3 h followed by re-annealing in air at 100 °C for 1 h (85361 Ω), and NNO thin films annealed with CaH_2 at 280 °C for 3 h followed by re-annealing in air at 200 °C for 3 h (30167 Ω), 6 h (19673 Ω), and 12 h (260 Ω).

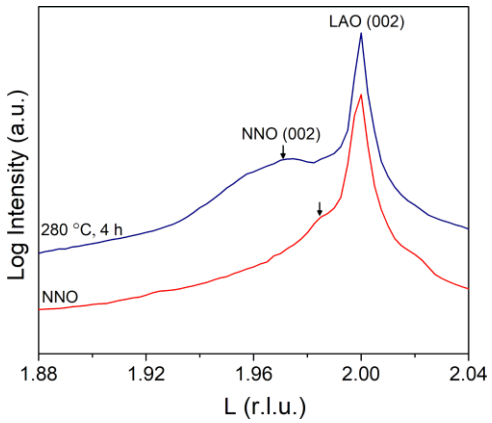

Fig. 6. Synchrotron XRD patterns of pristine NNO thin film and NNO thin film annealed with CaH_2 at 280 °C for 4 h. (002) reflection of LAO is labeled. (002) reflection of NNO is labeled with pseudocubic notation and indicated by an arrow. Pseudocubic lattice constant of LAO is used to define the reciprocal lattice unit (r.l.u). The shift of the (002) diffraction maximum of NNO to lower L values upon CaH_2 annealing reveals the lattice expansion due to strain induced by hydrogen doping.